Citation for published version:
Weller, M, Weber, O & Charles, B 2016, 'Phase Behaviour and Composition in the Formamidinium-Methylammonium Hybrid Lead Iodide Perovskite Solid Solution', *Journal of Materials Chemistry A*. https://doi.org/10.1039/C6TA06607K

DOI:
10.1039/C6TA06607K

Publication date:
2016

Document Version
Peer reviewed version

Link to publication

University of Bath

Alternative formats
If you require this document in an alternative format, please contact: openaccess@bath.ac.uk

General rights
Copyright and moral rights for the publications made accessible in the public portal are retained by the authors and/or other copyright owners and it is a condition of accessing publications that users recognise and abide by the legal requirements associated with these rights.

Take down policy
If you believe that this document breaches copyright please contact us providing details, and we will remove access to the work immediately and investigate your claim.

Download date: 26. Aug. 2022

Please do not adjust margins

Journal Name

ARTICLE

Phase Behaviour and Composition in the Formamidinium-Methylammonium Hybrid Lead Iodide Perovskite Solid Solution

Received 00th January 20xx,
Accepted 00th January 20xx

DOI: 10.1039/x0xx00000x

www.rsc.org/

O. J. Weber,[a] B. Charles[a] and M. T. Weller[a]

The phase behaviour of mixed A-site cation methylammonium (MA) / formamidinium (FA) lead iodide hybrid perovskites $FA_xMA_{1-x}PbI_3$ has been investigated using powder and variable temperature single crystal X-ray diffraction, with A site composition determined by ^{1}H solution NMR. At room temperature, the crystal class is cubic across the composition range $0.2 \leq x \leq 1$ but a tetragonal phase is observed for x = 0 ($MAPbI_3$) and x = 0.1. Cooling cubic $FA_xMA_{1-x}PbI_3$, $0.2 \leq x \leq 1$, phases below room temperature results in a phase change to a larger unit cell with tilted [PbI_6] octahedra and the temperature at which this occurs, $T_{C\rightarrow T}$, decreases sharply until x = 0.2 ($T_{C\rightarrow T}$ = 257 K) before steadily increasing to $T_{C\rightarrow T}$ = 283 K for $FA_{0.9}MA_{0.1}PbI_3$. The lattice parameters and optical band gap of cubic $FA_xMA_{1-x}PbI_3$, $0.2 \leq x \leq 1$ at 298 K have been shown to vary in accordance with Vegard's law, though a larger band gap is observed for the tetragonal phases, $0.0 \leq x \leq 0.1$.

Introduction

Lead halide hybrid perovskites have swiftly become an important class of materials for optoelectronic devices, most notably in high efficiency (>20%) thin film solar cells.[1] While the bulk of this intensive research has focused on methylammonium (MA) lead iodide (MAPI), increasing attention is being paid to formamidinium (FA) lead iodide (FAPI) and solid solutions between these two compounds. The ease of synthesis of A, B and X site solid solutions from the ABX_3 hybrid or inorganic perovskite family provides an effective and simple route to control their physical properties. Impressive solar cell efficiencies and greater stability, upon which successful deployment of hybrid perovskite technologies may well depend, have been reported for site-substituted solid solutions compared to the parent compounds.[2-5] Some of the highest cell efficiencies have been reported for MA/FA and I/Br mixtures (20.8%),[6] while triple A-site cation MA/FA/Cs, X-site I/Br, cells have displayed stabilised 18% power output for 250 hours.[7]

Despite the recent champion performance of mixed cation MA/FA solar cells, A-site mixtures are the least well studied system for any site-substitution within hybrid perovskites and remain poorly characterised with respect to their structure and true composition. This reflects the challenges of obtaining structural information on the organic components of hybrid perovskites using conventional laboratory X-ray sources in the presence of the heavy atoms Pb and I.

Recently the composition space of FA/MA and I/Br perovskites has been explored by Jacobsson et al.,[8] and Yang et al.,[9] who demonstrate the linear dependence of lattice parameter and band gap for FA/MA mixtures. However, in both cases the crystal systems of the thin film samples were not definitively determined and the compositions of as-deposited mixed cation / anion compounds were assumed, as throughout device literature, to reflect initial concentrations of the reactants in solution. In fact uptake of MA^+ and FA^+ and crystallisation of a solid solution $FA_xMA_{1-x}PbI_3$, $0 < x < 1$ may not reflect the solution concentrations. Furthermore incorporation of MA^+ and FA^+ cations may be strongly method dependent, resulting in notionally identical compounds with, in reality, very different optoelectronic performance. In addition, structure determination by powder X-ray diffraction is correspondingly more difficult for the thin, potentially highly oriented and textured films, used in solar cells, than for bulk materials.

FAPI and $FAPbI_yBr_{3-y}$ were originally characterised as adopting tetragonal unit cells,[10] and Noh et al. have reported a transition from tetragonal to cubic $MAPbI_yBr_{1-y}$ above y = 0.13.[11] The perovskite α-phase of FAPI has also been refined as trigonal from single crystal X-ray diffraction (SXD).[12] However, we have previously shown the structure of α-FAPI to be cubic at room temperature, space group *Pm-3m*, using high resolution neutron powder diffraction data, with the FA ion fully rotationally disordered,[13] a more recent SXD refinement study also adopts this cubic cell.[14] Neutron diffraction is far more sensitive to light atom positions than X-ray methods, for which the similarity of $[PbI_3]^-$ lattice between cubic and trigonal models generate near identical powder X-ray diffraction (PXD)

[a] Department of Chemistry and Centre for Sustainable Chemical Technologies, University of Bath, Claverton Down, Bath. BA2 7AY. UK. E-mail: m.t.weller@bath.ac.uk.

Electronic Supplementary Information (ESI) available: Reactant quantities used for crystal synthesis, Tables S1 & S2. SXD lattice parameters for every composition at 300 K, Table S3. NMR spectra, assignments and integrals, Fig. S1. PXD patterns for every composition, Fig. S2. CELREF unit cell refinements for $FA_{0.1}MA_{0.9}PbI_3$, Fig S3. Pawley fits to cubic Pm-3m PXD patterns, Fig S4. Pawley fits for tetragonal and cubic unit cells for $FA_{0.1}MA_{0.9}PbI_3$, Fig. S5. See DOI: 10.1039/x0xx00000x

Please do not adjust margins

Please do not adjust margins

patterns. MAPI, in contrast, is tetragonal at 298 K, adopting the space group *I4/mcm*, with a reduced lattice parameter splitting (c/√2×a) of approximately 1% and the organic cation disordered in the ab plane.[15] The a and c lattice vectors of tetragonal MAPI converge on heating to 327 K to form the cubic *Pm-3m* phase, with a fully disordered central organic cation.

The structural behaviour in the system $FA_xMA_{1-x}PbI_3$, 0 < x < 1, between the two end member phases MAPI and FAPI, has not previously been analysed in detail. However, this is of direct and crucial interest for the technological application of these materials due to the apparent increase in material stability and device performance of mixed cation systems. Density functional theory calculations[16] and calorimetric measurements[17] have revealed MAPI to have a positive enthalpy of formation with respect to disproportionation into its binary components PbI_2 and MAI, meaning that even with perfect protection from atmospheric conditions, devices with a single phase $MAPbI_3$ active layer may be fundamentally unstable in the long term. It is, however, notable that $MAPbI_3$ is readily formed from solid PbI_2 and MAI as soon as these components are brought into contact, suggesting experimentally this process to be energetically favourable. For a thermodynamically open system, MAPI decomposition to lead(II) iodide, methylamine and HI can occur via loss of volatile components, as evidenced by non-ambient X-ray diffraction and Knudsen effusion-mass spectrometry measurements at 60 °C.[18]

The high susceptibility of MAPI to hydrolytic degradation is well established.[19] A solar cell with effective encapsulation, or appropriate device layers, could both block water ingress and volatile perovskite component egress (as a closed system); however, other degradation pathways may still remain from chemical interaction of MAPI with the other device layers. Redox chemistry between metal (Ag, Al, Cr) contacts and MAPI has been shown to contribute to degradation in MAPI LEDs,[20] while the exact contribution of ion migration within MAPI to cell degradation remains to be better evaluated.

At the other end of the composition range, FAPI, a further problem is encountered. During the synthesis and deposition of cubic FAPI (α-phase), a competing yellow, non-perovskite δ-phase forms preferentially at room temperature, with the level generated dependent on the synthetic route and local chemical / strain environment. Theory has indicated that MA/FA solid solutions should be thermodynamically more stable,[16] and form the perovskite α-phase at room temperature with no competing non-perovskite δ-phase, which is indeed observed experimentally.[21] Such materials would be strongly preferred for technological applications, as is becoming increasingly apparent in the device literature, including high efficiency solar cells[2,5,6] and nanowire lasers.[3] Solid solutions of $FA_xCs_{1-x}PbI_3$ have similarly displayed stabilisation of the cubic perovskite phase, with respect to the room temperature non-perovskite phases of the parent compounds.[22] A further aspect of solar cell devices is that for many applications they will need to operate over a large temperature range and so an understanding of changes in structure, and therefore optoelectronic properties, of the absorber material as a function of temperature is needed.

Herein we report the detailed analysis of mixed cation structures in the $FA_xMA_{1-x}PbI_3$ x = 0 - 1.0 system using variable temperature single crystal (VT-SXD) and powder (PXD) X-ray diffraction, solution NMR analysis of composition and UV-Vis spectroscopy. Two different methods for preparing the hybrid perovskites in this solid solution, namely precipitation from aqueous hydroiodic acid and inverse solubility crystallisation in γ-butyrolactone, have been employed and the compositions and lattice parameters are compared to ensure equivalence between the two methods. Materials with the nominal compositions, based on the reactant concentrations, $FA_xMA_{1-x}PbI_3$ 0 ≤ x ≤ 1, with x in 0.1 increments, were synthesised using the two routes described in the Experimental Section. The product phases are denoted $FA_xMA_{1-x}PbI_3$ (HI), obtained from cooling in HI, and $FA_xMA_{1-x}PbI_3$ (IS), obtained from inverse solubility in γ-butyrolactone, respectively. Actual product compositions were determined after dissolution by solution ^{1}H NMR.

Experimental

Materials Synthesis

All reagents were purchased from Sigma Aldrich, solvents from Alfa Aesar, unless otherwise noted.

Precursor synthesis of methylammonium iodide (MAI) was carried out. 16.620 mL hydroiodic acid (57 wt%, +1.5wt% H_3PO_2 stabiliser) was added dropwise to 10.891 mL of methylamine (40 wt % in H_2O) in an ice bath under stirring. After 2 hours H_2O was removed by rotary evaporation and the product was recrystallised from hot ethanol to remove impurities, potentially introduced from H_3PO_2, washed with diethyl ether and oven dried. Formamidinium iodide (FAI) was synthesised in analogous manner using 12.108 g of formamidinium acetate dissolved in 100 mL ethanol, to which 15.36 mL HI was added.

Crystal growth by precipitation from HI Mixed cation perovskites, $MA_xFA_{1-x}PbI_3$, were prepared based on the method of Polglitsch and Weber.[23] Methylammonium iodide, formamidinium iodide and lead acetate trihydrate were added to HI(+1.5wt% H_3PO_2) at 1M concentration. The solution was heated under nitrogen to 100°C. The temperature was then gradually lowered to 46°C. The precipitate of black perovskite crystals was filtered and oven dried at 100 °C overnight. Average yield 55%. Full details of the reaction compositions are provided in the ESI, Table S1.

This journal is © The Royal Society of Chemistry 20xx

Please do not adjust margins

Please do not adjust margins

Crystal growth by inverse solubility in γ-butyrolactone: following the method of Saidaminov et al.[24] Methylammonium iodide, formamidinium iodide and lead iodide were dissolved at 60°C in γ-butyrolactone at 1M concentration, filtered using 0.22µm filters and placed in clean vials. The solutions were initially heated to 110°C, the temperature was then increased to 120 °C for 1 hour before the solution was filtered and crystals dried in an oven at 100 °C overnight. Full details of the reaction compositions are provided in the ESI, Table S2.

Characterisation Methods

Single crystal X-ray diffraction data were collected on an Agilent SuperNova dual tube Eos S2 CCD diffractometer operating graphite monochromated Mo-Kα (λ = 0.7093 Å) radiation. Variable temperature data were collected in 5 or 15 K steps from 300 K to 150 K. A dwell time of two minutes before each data collection was introduced to ensure a stable temperature. Structure solution and refinement was carried out in WinGX using XPREP and SHELXS-2013 to solve structures by direct methods and SHELXL-2013 for structure refinement.

Powder diffraction patterns were collected on Bruker Advance D8 diffractometer using Cu_{Ka1} radiation λ = 1.54060 Å. CELREF (LMPG)[25] was used to fit peak positions and to refine a cubic unit cell parameter, in space group *Pm-3m*. A zero point error on each dataset was refined simultaneously with the lattice parameter. Indexing, peak fitting and Pawley refinement were carried out in TOPAS Academic. NMR spectra were collected on an Agilent 300 MHz NMR spectrometer and the spectra were analysed in MNova (Mestrelab). 5 mg of the perovskite was dissolved in d_6-DMSO and the MA/FA ratio within each by comparison of the integrals of the NH_3 group peak of MA (7.47, s) to the NH_2 peaks of FA (8.65, d; 8.99, s).

Results and discussion

Comparison of Synthesis Methods

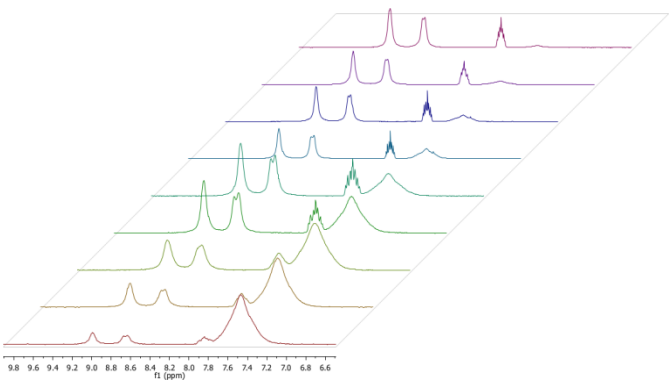

Figure 1 Sections from ^{1}H solution NMR for $FA_xMA_{1-x}PbI_3$ (HI), for x = 0.1 (bottom) to x = 0.9 (Top) in 0.1 increments. Assignments for MA^+: ^{1}H NMR (300 MHz, d6-DMSO) δ 7.46 (3H, NH_3). FA^+: ^{1}H NMR (300 MHz, d6-DMSO) δ 7.83 (1H, tt, CH), 8.63 (2H, d, NH_2), 8.98 (2H, s, NH_2).

x=FA	MA:FA integral ratio			Stoichiometry		
	theo.	HI(obs)	IS(obs)	theo.	HI(obs)	IS(obs)
0.1	9.000	7.98	9.16	$FA_{0.1}MA_{0.9}PbI_3$	$FA_{0.11}MA_{0.89}PbI_3$	$FA_{0.10}MA_{0.90}PbI_3$
0.2	4.000	3.79	4.70	$FA_{0.2}MA_{0.8}PbI_3$	$FA_{0.21}MA_{0.79}PbI_3$	$FA_{0.18}MA_{0.82}PbI_3$
0.3	2.333	2.53	2.74	$FA_{0.3}MA_{0.7}PbI_3$	$FA_{0.28}MA_{0.72}PbI_3$	$FA_{0.27}MA_{0.73}PbI_3$
0.4	1.500	1.50	1.66	$FA_{0.4}MA_{0.6}PbI_3$	$FA_{0.40}MA_{0.60}PbI_3$	$FA_{0.38}MA_{0.62}PbI_3$
0.5	1.000	0.86	1.07	$FA_{0.5}MA_{0.5}PbI_3$	$FA_{0.54}MA_{0.46}PbI_3$	$FA_{0.48}MA_{0.52}PbI_3$
0.6	0.667	0.68	0.63	$FA_{0.6}MA_{0.4}PbI_3$	$FA_{0.59}MA_{0.41}PbI_3$	$FA_{0.61}MA_{0.39}PbI_3$
0.7	0.429	0.41	0.45	$FA_{0.7}MA_{0.3}PbI_3$	$FA_{0.71}MA_{0.29}PbI_3$	$FA_{0.69}MA_{0.31}PbI_3$
0.8	0.250	0.24	0.22	$FA_{0.8}MA_{0.2}PbI_3$	$FA_{0.81}MA_{0.19}PbI_3$	$FA_{0.82}MA_{0.18}PbI_3$
0.9	0.111	0.12	0.09	$FA_{0.9}MA_{0.1}PbI_3$	$FA_{0.89}MA_{0.11}PbI_3$	$FA_{0.92}MA_{0.08}PbI_3$

Solution ^{1}H NMR spectra obtained from dissolved $FA_xMA_{1-x}PbI_3$ crystals are displayed in Figure 1 and the full spectra, integrals and multiplet assignments for MAPI, FAPI and $FA_{0.5}MA_{0.5}PbI_3$ are plotted in the ESI Fig. S1. The ratio of peak integrals of the characteristic MA and FA cation resonances were compared for each spectrum to determine the stoichiometry of the compound (Table 1). For example for the target x = 0.1 ($FA_{0.1}MA_{0.9}PbI_3$), the theoretical ratio of the NMR integrals of the proton resonances for MA:FA is 0.9/0.1 = 9, while the experimentally observed ratios determined from [NH_3/3]/[(NH_2+NH_2)/4)], were found to be 7.98 (HI) and 9.16 (IS), giving x (FA) = 0.11 (HI) and 0.10 (IS). The predicted stoichiometry based on reactant concentration is very close to the ratio of the two organic cations by NMR, within ± 0.04 of ideal stoichiometry for every composition.

Single Crystal X-ray Diffraction

The inverse, or retrograde, solubility (IS) crystallisation enabled the growth of large (a few millimetres in each dimension) crystals across the full composition range. Single crystals could also be grown by precipitation from HI, though a prolonged cooling ramp from 100 °C to 46 °C (to avoid hydrate formation in the case of MAPI) is required to grow crystals suitable for single crystal diffraction. For the HI method the crystallite size tended to decrease with increasing formamidinium content. Single crystal X-ray diffraction data were obtained at 300 K for $FA_xMA_{1-x}PbI_3$, 0 < x < 1, IS method, with the lattice parameter tending to increase along with the amount of the larger organic FA cation (ESI, Table S3). For the solid solution compositions $FA_xMA_{1-x}PbI_3$, 0.2 < x < 1, a cubic unit cell with dimensions of approximately 6.3 Å was obtained from the single crystal diffraction data at 300 K. For $FA_{0.1}MA_{0.9}PbI_3$, the 300 K data showed additional reflections and these were preliminarily indexed using a larger, doubled, 12.6 Å cubic unit cell.

Variable temperature single crystal diffraction (VT-SXD) was used to investigate the phase behaviour of solid solutions. Initial experiments were carried out on $FA_{0.5}MA_{0.5}PbI_3$. SXD was carried out in 5 K steps on cooling from 300 K to 150 K. The reduced lattice parameters of $FA_{0.5}MA_{0.5}PbI_3$, as a function of temperature, are plotted in Fig. 2a. A doubling of unit cell

Figure 2 (a) VT-SXD $FA_{0.5}MA_{0.5}PbI_3$ reduced lattice parameters and cell volume, cooled from 300 K to 150 K in 5 K steps. (b) SXD patterns displaying the hk0 plane reflections for $FA_{0.2}MA_{0.8}PbI_3$ at 300 K (6.3 Å unit cell) and 150 K (12.6 Å unit cell). (c) Variation in phase transition temperature from 6.3 Å to 12.6 Å unit cell with composition.

Please do not adjust margins

Please do not adjust margins

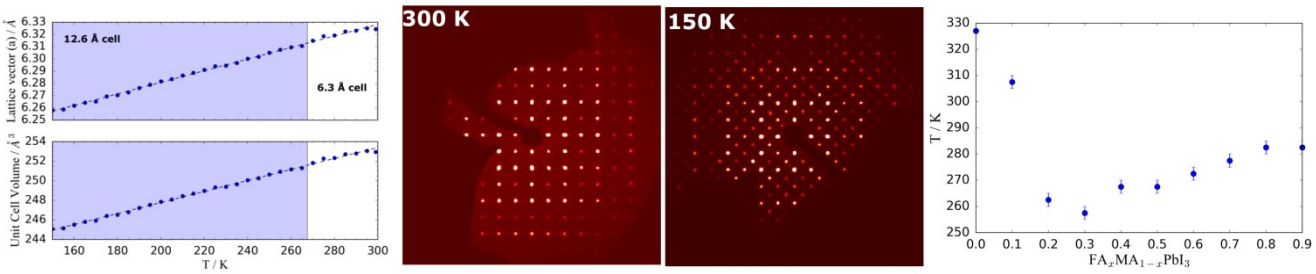

parameters for this composition was observed on cooling from 265 to 260 K.

Thermal expansion coefficients are readily extracted from the linear temperature dependence of the cell parameters and volume. For $FA_{0.5}MA_{0.5}PbI_3$ these were found to be a_L = 7.9 x 10^{-4} K^{-1} for the linear thermal expansion along the lattice vector a (all three directions equivalent for a cubic cell) and a_V = 2.2 x 10^{-4} K^{-1} for the volumetric expansion coefficient. The expression for the volumetric coefficient is given in Equation 1. The values obtained are higher than the values reported for pure $MAPbI_3$ from powder XRD,[26] which as noted in this reference are up to an order of magnitude higher than typical solar cell substrate materials.

Further variable temperature experiments SXD were carried out in 5 K steps for all other IS synthesis route samples, $FA_xMA_{1-x}PbI_3$, 0 < x < 1, to identify and locate any phase transition temperature for each composition. On cooling, weak additional diffraction spots in the 0kl, h0l and hk0 planes appear at intervals halfway between those of the cubic cell of the 300 K pattern for each composition, indicating formation of a larger unit cell expanded from the high temperature 6.3 Å cubic perovskite phase (Fig. 2b) and suggesting an additional degree of ordering within the low temperature structures. It was found from the VT-SXD patterns that the transition temperature decreases sharply for samples with x ≤ 0.2 across the rest of the composition range the transition temperature, but then

$$a_V = \frac{1}{V}\frac{\partial V}{\partial T} \qquad (1)$$

recovers to gradually rise back towards room temperature, Fig. 2c.

Powder X-ray diffraction

Powder X-ray diffraction (PXD) generally provides less structural information than SXD (where suitable crystals exist). However, ambiguities can arise in the analysis of SXD data for the correct identification of the crystal system after a crystal has undergone twinning caused by a phase transition. In such cases analysis of PXD data can provide a more rapid and clear-cut identification of the crystal system.

PXD patterns ($Cu_{K\alpha}$ radiation, 28° ≤ 2θ ≤ 33°) for the phases with 0 ≤ x ≤ 0.3 (HI) are shown in Fig. 3a; full patterns for all compositions are plotted in the ESI (Fig. S2). In the powder pattern of MAPI, well known to be tetragonal at room temperature, the clear splitting of diffraction peaks at 28.5°, the (004)/(220) reflection pair, and 32° is observed, along with the {213} reflection at 31.1°. For the x = 0.1 structure, a weak reflection is seen at θ = 31.2° and obviously "broader" peaks at 28.5 and 32°, this suggests that a tetragonal cell still exists at room temperature for x = 0.1 in $FA_{0.1}MA_{0.9}PbI_3$.

Indexing the x = 0.1 PXD data in *TOPAS* Academic suggested tetragonal *I4cm*, cubic *F23* and trigonal *R3* cells with high figures of merit. The room temperature tetragonal phase of MAPI crystallises in *I4/mcm* (it should be noted that tetragonal space groups *I4cm*, *I4/mcm* and *I-4c2* all have identical reflection conditions and hence generate identical hkl possibilities in PXD patterns). The predicted diffraction pattern peak positions in CELREF are shown in the ESI Fig. S3. The reduced lattice

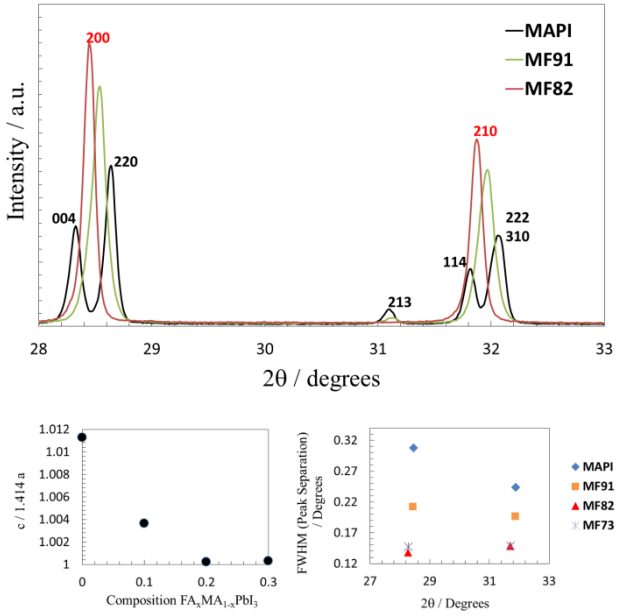

Figure 3 (a) Room temperature powder X-ray diffraction patterns 28-34° 2θ for MAPI (black), $FA_{0.9}MA_{0.1}PbI_3$ (MF91, yellow) and $FA_{0.2}MA_{0.8}PbI_3$ (MF82, red). The solid solutions 1 > x > 0.1 display no tetragonal peak splitting and no {213} peak at 31.1° 2θ (inconsistent with cubic symmetry). (b) Reduced lattice parameter ratio from a Pawley fit to the diffraction patterns 0 ≤ x ≤ 0.3. (c) FWHM of pseudo-Voight peak fits to individual peaks for 0.1 ≤ x ≤ 0.3 and peak-peak separation of {004} to {220} reflections for x = 0 MAPI.

parameter ratio, γ = (c/√2×a), of Pawley fits to the data using tetragonal *I4cm* is displayed in Fig. 3b. Full pattern Pawley fits for 0.1 ≤ x ≤ 0.3 are plotted in the ESI Figs. S4-5. The reduced lattice parameter ratio shows that while for MAPI γ = 1.01, $FA_{0.1}MA_{0.9}PbI_3$ γ = 1.003 and $FA_{0.2}MA_{0.8}PbI_3$ γ= 1.0002 as the value tends to 1, within the resolution (Δd/d) of the diffractometer, i.e. a cubic cell exists for x ≥ 0.2. Further confirmation of a tetragonal unit cell for $FA_{0.1}MA_{0.9}PbI_3$ was obtained from the measured peak half-widths. Fig. 3c plots the

This journal is © The Royal Society of Chemistry 20xx

Please do not adjust margins

Please do not adjust margins

full width, half height maximum for pseudo-Voigt functions fit to individual peaks in the powder patterns 0.1 ≤ x ≤ 0.3 and the peak-peak separation for the {004} to {220} reflections in x = 0 MAPI. A clear trend is observed in which the peak width tends to a constant value (the instrumental peak width of ~0.12°) by x = 0.2, with "broader" peak widths obtained for the x = 0.1 pattern as the program attempts to fit the two close reflections in tetragonal $FA_{0.1}MA_{0.9}PbI_3$.

Crystal systems and unit cell parameters in the $FA_xMA_{1-x}PbI_3$ solid solution

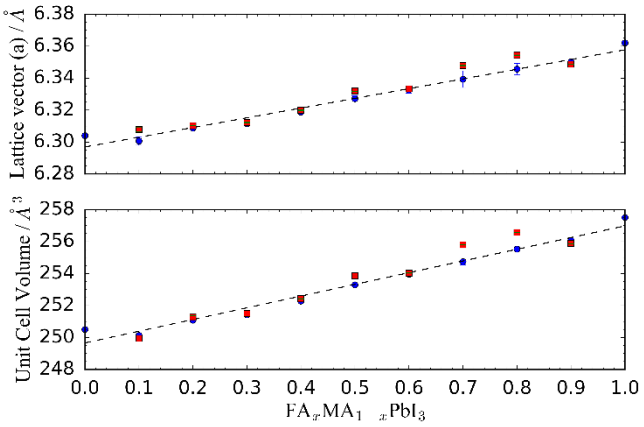

Figure 4 Reduced lattice parameter for $MAPbI_3$ and $FA_{0.1}MA_{0.9}PbI_3$ (tetragonal values are approximately √2a, √2a and 2a) and cubic lattice parameters for $FA_xMA_{1-x}PbI_3$, x ≥ 0.2, in x = 0.1 increments. Bottom – unit cell volume expansion across the same composition range. The data for the terminal compositions, i.e. $FAPbI_3$ and $MAPbI_3$, are taken from neutron powder diffraction data (NPD) on HRPD at ISIS for $FAPbI_3$[13] and from D20 at ILL for $MAPbI_3$.[14] PXD for HI powders – blue circles. SXD for IS single crystals – red squares. Error bars are the esd from the least squares fit in CELREF for PXD data, esd errors for the SXD measurements lie within the data points.

Assignment of the correct crystal system and space group to the low temperature phase of phases $FA_xMA_{1-x}PbI_3$ using just X-ray diffraction data needs to be undertaken with caution. While the SXD data obtained from $FA_{0.1}MA_{0.9}PbI_3$ at 300 K are best indexed using a 12.6 Å cubic cell (and that from all other compositions below $T_{C\rightarrow T}$), the room temperature PXD pattern for $FA_{0.1}MA_{0.9}PbI_3$ provides evidence that a tetragonal cell is the correct choice for this system. The lower temperature structure is derived from the higher temperature 6.3 Å cubic cell; with a 2a × 2a × 2a for the cubic crystal system (a = ~12.6 Å) or √2a x √2a x 2c unit cell for the closely related tetragonal description.

For hybrid perovskites, X-ray scattering is dominated by the heavy atom framework lead and iodine, with little contribution from the organic cations, which are further dynamically disordered over several orientations. We have routinely observed twinning in the SXD patterns of hybrid perovskite crystals as they are cooled through phase transition temperatures. Data obtained from multiply twinned crystals leads to further problems in extracting the correct lattice parameters and crystal system, as has been seen with the original trigonal crystal system assignment of FAPI.[12]

Unit cell refinements of the room temperature powder diffraction data (Fig. 4) for the MA/FAPI (HI) samples were carried out in CELREF.[25] These display a very near linear increase in reduced lattice parameter and volume as composition is varied across the series and the amount of the larger FA cation increases. The agreement in reduced lattice parameter between these X-ray data (0.1 < x < 0.9) and neutron data for $MAPbI_3$ (D20, ILL)[15] and $FAPbI_3$ (HRPD, ISIS)[13] is excellent. The room temperature unit cells and cell volumes for IS crystals, determined by SXD (Table ESI S3), are included for comparison of the two synthesis methods, with lattice parameters displaying very close agreement.

UV-vis Spectroscopy

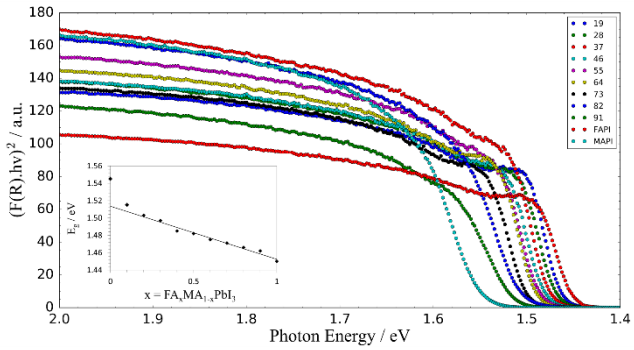

Figure 5 Tauc plot of UV-vis reflectance spectra for each composition (HI). Inset: variation of band gap with composition from extrapolation of the linear part of increasing absorbance. Inset – absorption onset variation with composition. A linear trend line for 0.2 ≤ x ≤ 1 is extrapolated to demonstrate the deviation for tetragonal x = 0.1 and 0.

Solid state reflectance UV-vis spectroscopy data revealed a linear decrease in optical band gap with increasing FA content from 0.2 ≤ x ≤ 1 (Fig. 5), i.e. the range of compositions adopting a cubic unit cell at room temperature. The overall shift in the band gap of 100 meV across the whole composition range is much smaller than for B or X site substitution, which is unsurprising given the lack of contribution of the A site cation to the density of states close to valence or conduction band edges.[27-29]

A band gap for MAPI of 1.55 eV was obtained from the Tauc plot, by extrapolation of the linear component of the absorption onset, entirely consistent with previous published values for bulk materials[30] and slightly smaller than the values for thin films.[8] Absorption onset is also markedly sharper for cubic solid solution compositions 0.2 ≤ x ≤ 1. MAPI (x = 0) shows the greatest deviation from the linear trend in the optical band gap absorption onset, with the R^2 value for a linear least squares fit to the data increasing from 0.91 to 0.98 upon exclusion of tetragonal MAPI and x = 0.1 from the dataset (Fig. 5, inset).

The deviation from this trend for MAPI and $FA_{0.1}MA_{0.9}PbI_3$ reflects the dependence of hybrid perovskite band gaps on Pb-I-Pb bonding angle,[31,28,29] with tetragonal MAPI tilted $a^0a^0c^-$ in Glazer notation. In this work we now observe this behaviour for $FA_{0.1}MA_{0.9}PbI_3$ as can be seen in Fig. 5 (inset) where the absorption onset lies at a slightly higher energy than would be expected from linear extrapolation of the data from the cubic

Please do not adjust margins

Please do not adjust margins

$FA_xMA_{1-x}PbI_3$, 0.2 ≤ x ≤ 1 compounds. The observed shift in absorption edge to longer wavelengths (smaller band gap) with increasing FA content is monotonic across the cubic range 0.2 ≤ x ≤ 1; across this same compositional range the lattice parameter increase follows Vegard's Law. In contrast, MAPI has been found to possess a positive band gap temperature coefficient, i.e. an increase in band gap is observed with increasing temperature as the lattice parameter expands.[32,33] How this behaviour relates to the variable temperature optical behaviour in solid solutions remains to be established, but it is probably related to increased thermal vibration and local tilting of the PbI_6 octahedra.

Formally, in the room temperature *Pm-3m* phases $FA_xMA_{1-x}PbI_3$ 0.2 ≤ x ≤ 1, all the Pb-I-Pb angles are fixed at 180° so no dependence of the band gap on this measured bond angle would be expected. Diffraction data provide a time and space averaged representation of these materials, while the local and dynamic structure are likely to contribute to the observed optical behaviour. The impact of such local structure effects on the electronic structure, and therefore optical properties, in these materials is a topic for further theoretical and experimental development. In the $FA_xMA_{1-x}PbI_3$, 0.2 ≤ x ≤ 1 compounds it is possible that that the PbI_3 framework becomes more rigid with increasing levels of the larger $[FA]^+$ cation and this reduces the band gap, despite the overall increase in lattice parameter.

Discussion

These results, demonstrating phase-pure solid solutions from $FA_xMA_{1-x}PbI_3$, 0.0 ≤ x ≤ 1, disagree with some of the observations reported in the literature. Binek et al.[21] studied inclusion of MA^+ in $FA_xMA_{1-x}PbI_3$ via solvent cation exchange with 5-15% MAI in FAI solution, reporting no significant shift in the lattice parameter upon increasing MAI concentration. However, analysis of final perovskite composition was not reported to establish correspondence to the starting solution ratios and herein we have shown that the lattice parameter varies linearly across the whole composition range, in agreement with the findings of Yang et al.,[9] who however observed partial formation of δ-FAPI for x ≥ 0.6 for thin films on ITO, indicating non-uniformity of the cation distribution in the films, while we observe no secondary phase formation, except for pure FAPI.

The stoichiometry and defect structure in each compound may depend on the idiosyncrasies of the synthesis method, particularly the chemical potential of the reactants and the crystallisation dynamics, which are drastically different between the iodide rich HI crystal growth and thin film deposition from stoichiometric solutions, a 3:1 excess of the organic iodide versus PbI_2, or a two-step deposition with a large excess of organic iodide in the second step. The two methods employed in this study both depend on crystallisation from stoichiometric solutions due to a reduction in solubility as the temperature changes. Inverse solubility is an unusual effect in which hybrid perovskites display significant loss of solubility upon heating in certain solvents.[24,34,35] This effect is highly solvent and compound specific and results in rapid crystal growth as the temperature is raised. Heterovalent dopant inclusion, e.g. Bi^{3+} for Pb^{2+}, has also been demonstrated by the same method.[36] The temperature required to induce crystallisation can be reduced by solvent engineering by adding up to 30 wt% chlorobenzene to the γ-butyrolactone.[37]

The phase behaviour of the $FA_xMA_{1-x}PbI_3$ system as a function of temperature has not previously been explored. We have shown using VT-SXD that a phase transition from cubic occurs on cooling a little below room temperature across the complete compositional range, 0.2 ≤ x ≤ 0.9. In the case of $FA_{0.1}MA_{0.9}PbI_3$ the phase transition temperature ($T_{C\rightarrow T}$) takes place slightly above room temperature so that the PXD pattern collected at 298 K shows reflections that require indexing using a tetragonal unit cell. For all compositions the SXD data obtained below $T_{C\rightarrow T}$ are best indexed using a doubled (~12.6 Å) cubic unit cell, though an I-centred tetragonal cell can also be used but yields a higher R_{int}. In both cases it is likely that the increased unit cell size results from tilting of the Pb-I octahedra. However, the dominance of X-ray scattering from the heavy atom inorganic framework, with minimal information on the orientations of the organic cations, means that it is not possible to definitively distinguish between the different crystal systems from the SXD data. We believe that the lattice parameter ratios, peak broadening and additional reflections observed in the room temperature PXD data (Fig. 3) provides the strongest evidence for a tetragonal structure for the low temperature phase of $FA_{0.1}MA_{0.9}PbI_3$.

It is apparent from the data presented herein that only a small amount of FA inclusion into MAPI, between 0.1 ≤ x ≤ 0.2, is required to induce a change from tetragonal to cubic perovskite structure, at room temperature. Using the approach of Kieslich et al.[38] to estimate the effective radius of organic cations, MA r_{eff} = 217 pm and FA r_{eff} = 253 pm, to calculate a tolerance factor, as routinely undertaken for perovskite oxides, we find that α = 0.91 for $MAPbI_3$ versus 0.98 for $FAPbI_3$. Inorganic ionic radii used were $r_{Pb(II)}$ = 119 pm and $r_{I(-I)}$ = 220 pm, from Shannon's tables for halides.[39] Since it is commonly assumed that for 0.81 < α < 1.01 the perovskite structure is observed, this approach is clearly insufficient for explaining the formation of δ-$FAPbI_3$ and the structural dissimilarities between $MAPbI_3$ and $FAPbI_3$. The shape and hydrogen bonding capabilities of each organic species, not captured by the spherical ion assumption in the Goldschmidt tolerance equation, are theorised to play crucial roles in the structural evolution of these and related hybrid compounds.[40]

Recent DFT calculations suggest that in the absence of H-bonding the structure of MAPI would be cubic.[41] For all compositions, 0 ≤ x ≤ 0.9, the materials tend towards cubic perovskite symmetry (with a fully disordered A-site cation orientation) as the temperature increases. This behaviour is associated with an expansion in the lattice parameters and changes in the hydrogen bonding between the organic cation hydrogen atoms and the iodide ion of the inorganic lattice – an interaction which becomes an increasingly unimportant compared to thermal energy and motion. The disruption of hydrogen bonding due to the introduction of two different organic cations, MA and FA, with dissimilar hydrogen bonding

This journal is © The Royal Society of Chemistry 20xx

Please do not adjust margins

Please do not adjust margins

strengths, directionality and acidities (FA being less acidic), may be a factor in determining the temperature profile of the phase transition as the cation ratio is changed across the series.

The estimation of effective ionic radii presents another complication for hybrid halide perovskites over and above their inorganic counterparts. Recently Travis et al.[42] have derived ionic radii for heavy metal halides, noting the differences from Shannon radii for large, less electronegative ions and define a revised tolerance space for hybrid halide perovskites. Suppression of the δ-phase of $CsPbI_3$/$FAPbI_3$ has been studied in terms of the mixing entropy contribution to the free energy of each phase, with entropic stabilisation of the α-phase perovskite for mixed Cs/FA calculated to be on the order of 0.05 eV.[22]

Conclusions

Uptake of MA^+ and FA^+ cations from solution into bulk phase crystals of $FA_xMA_{1-x}PbI_3$ has been shown to be statistical for two different synthesis methods − crystallisation from hydroiodic acid and inverse solubility in γ-butyrolactone. Phases formed with $x \geq 0.2$ in the $FA_xMA_{1-x}PbI_3$ solid solution are cubic at room temperature, but for x = 0.1 and x = 0 a tetragonal phase is observed. In the mixed cation systems no transition to a non-perovskite δ-phase is observed immediately following the synthesis, except for x = 0, FAPI, which begins to partially decompose to δ-FAPI, as previously reported.[13] The lattice parameters and optical band gap of $FA_xMA_{1-x}PbI_3$, $0.2 \leq x \leq 1$ at 298 K vary in accordance with Vegard's law, but with a larger band gap observed for the tetragonal phase, $0.0 \leq x \leq 0.1$.

The results presented here summarise a robust and simple means to determine the A-site cation composition, and therefore band gap, of $FA_xMA_{1-x}PbI_3$ solid solutions from refined lattice parameters derived from PXD data.

For every composition in the $FA_xMA_{1-x}PbI_3$ system a phase transition is observed upon cooling the sample (from above room temperature for x = 0 and 0.1). X-ray diffraction data obtained below the transition temperature may, in all cases, be indexed using a tetragonal or doubled cubic unit cell. However, distinguishing different possible structures for the low temperature phase for $x \geq 0.1$ from X-ray diffraction data alone is not possible due to the dominance of the scattering by the heavy atoms Pb and I. Future planned low temperature neutron diffraction studies of phases in the $FA_xMA_{1-x}PbI_3$, $0.1 \leq x \leq 1.0$ should help resolve the low temperature structures of these materials

Acknowledgements

OJW and BC would like to thank the EPSRC for PhD and M.Res. studentship funding via the EPSCRC doctoral training centre in Sustainable Chemical Technologies (EP/G03768X/1, EP/L016354/1) and also Dr. Mary Mahon, University of Bath, for help and advice on crystallography.

Notes and references

1 W. S. Yang, J. H. Noh, N. J. Jeon, Y. C. Kim, S. Ryu, J. Seo, and S. I. Seok, *Science*, 2015, **348**, 1234–1237.
2 M. Hu, L. Liu, A. Mei, Y. Yang, T. Liu, and H. Han, *J. Mater. Chem. A*, 2014, **2**, 17115–17121.
3 Y. Fu, H. Zhu, A. Schrader, D. Liang, Q. Ding, P. Joshi, L. Hwang, X.-Y. Zhu, and S. Jin, *Nano Lett.*, 2016, **16**, 1000–1008.
4 N. Pellet, P. Gao, G. Gregori, T.-Y. Yang, M. K. Nazeeruddin, J. Maier, and M. Grätzel, *Angew. Chem. Int. Ed. Engl.*, 2014, **53**, 3151–7.
5 N. J. Jeon, J. H. Noh, W. S. Yang, Y. C. Kim, S. Ryu, J. Seo, and S. Il Seok, *Nature*, 2015, **517**, 476–480.
6 D. Bi, W. Tress, M. I. Dar, P. Gao, J. Luo, C. Renevier, K. Schenk, A. Abate, F. Giordano, J.-P. Correa Baena, J.-D. Decoppet, S. M. Zakeeruddin, M. K. Nazeeruddin, M. Gratzel, and A. Hagfeldt, *Sci. Adv.*, 2016, **2**, e1501170–e1501170.
7 M. Saliba, T. Matsui, J.-Y. Seo, K. Domanski, J.-P. Correa-Baena, N. Mohammad K., S. M. Zakeeruddin, W. Tress, A. Abate, A. Hagfeldt, and M. Grätzel, *Energy Environ. Sci.*, 2016. Advance Article.
8 J. T. Jacobsson, J. P. Correa Baena, M. Pazoki, M. Saliba, K. Schenk, M. Grätzel, and A. Hagfeldt, *Energy Environ. Sci.*, 2016, **9**, 1706–1724.
9 Z. Yang, C.-C. Chueh, P.-W. Liang, M. Crump, F. Lin, Z. Zhu, A. K. –Y. Jen, *Nano Energy*, 2016, **22**, 328-337
10 G. E. Eperon, S. D. Stranks, C. Menelaou, M. B. Johnston, L. M. Herz, and H. J. Snaith, *Energy Environ. Sci.*, 2014, **7**, 982-988.
11 J. H. Noh, S. H. Im, J. H. Heo, T. N. Mandal, S. I. Seok, *Nano Lett.*, 2013, **4**, 1764-1769
12 C. C. Stoumpos, C. D. Malliakas, and M. G. Kanatzidis, *Inorg. Chem.*, 2013, **52**, 9019–38.
13 M. T. Weller, O. J. Weber, J. M. Frost, and A. Walsh, *J. Phys. Chem. Lett.*, 2015, **6**, 3209–3212.
14 A. A. Zhumekenov, M. I. Saidaminov, M. A. Haque, E. Alarousu, S. P. Sarmah, B. Murali, I. Dursun, X.-H. Miao, A. L. Abdelhady, T. Wu, O. F. Mohammed, and O. M. Bakr, *ACS Energy Lett.*, 2016, **1**, 32–37.
15 M. T. Weller, O. J. Weber, P. F. Henry, A. M. Di Pumpo, and T. C. Hansen, *Chem. Commun.*, 2015, **51**, 4180–4183.
16 Y.-Y. Zhang, S. Chen, P. Xu, H. Xiang, X.-G. Gong, A. Walsh, and S.-H. Wei, 2015, arXiv:1506.01301 [cond-mat.mtrl-sci]
17 G. P. Nagabhushana, R. Shivaramaiah, and A. Navrotsky, Proc. Natl. Acad. Sci., 2016, **113**, 7717–7721.
18 B. Brunetti, C. Cavallo, A. Ciccioli, G. Gigli, and A. Latini. *Sci. Reports*, 2016, **6**, 6050–6051.
19 A. M. A. Leguy, Y. Hu, M. Campoy-Quiles, M. I. Alonso, O. J. Weber, P. Azarhoosh, M. van Schilfgaarde, M. T. Weller, T. Bein, J. Nelson, P. Docampo, P. R. F. F. Barnes, M. van Schilfgaarde, M. T. Weller, T. Bein, J. Nelson, P. Docampo, and P. R. F. F. Barnes, *Chem. Mater.*, 2015, **27**, 3397–3407.
20 L. Zhao, R. A. Kerner, Z. Xiao, Y. L. Lin, K. M. Lee, J. Schwartz, and B. P. Rand, *ACS Energy Lett.*, 2016, **1**, 595–602.
21 Binek, F. C. Hanusch, P. Docampo, and T. Bein, *J. Phys. Chem. Lett.*, 2015, **6**, 1249–1253.
22 Yi, J. Luo, S. Meloni, A. Boziki, N. Ashari-Astani, C. Grätzel, S. M. Zakeeruddin, U. Rothlisberger, and M. Grätzel, *Energy Environ. Sci.*, 2015, **9**, 656–662.
23 A. Poglitsch and D. Weber, *J. Chem. Phys.*, 1987, **87**, 6373.
24 M. I. Saidaminov, A. L. Abdelhady, B. Murali, E. Alarousu, V. M. Burlakov, W. Peng, I. Dursun, L. Wang, Y. He, G. Maculan, A. Goriely, T. Wu, O. F. Mohammed, and O. M. Bakr, *Nat. Commun.*, 2015, **6**, 7586.
25 *LMGP-Suite Suite of Programs for the interpretation of X-ray Experiments, by Jean laugier and Bernard Bochu, ENSP/Laboratoire des Matériaux et du Génie Physique, BP 46. 38042 Saint Martin d'Hères, France.*

Please do not adjust margins

Please do not adjust margins

26 J. T. Jacobsson, J. L. Schwan, M. Ottosson, A. Hagfeldt, T. Edvinsson, *Inorg. Chem.*, 2015, **54**, 10678-85.
27 F. Brivio, K. T. Butler, A. Walsh, and M. Van Schilfgaarde, *Phys. Rev. B.*, 2014, **89**, 155204.
28 I. Borriello, G. Cantele, and D. Ninno, *Phys. Rev. B*, 2008, **77**, 235214.
29 T. Umebayashi, K. Asai, T. Kondo, and A. Nakao, *Phys. Rev. B*, 2003, **67**, 155405.
30 A. Leguy, P. Azarhoosh, M. I. Alonso, M. Campoy-Quiles, O. J. Weber, J. Yao, D. Bryant, M. T. Weller, J. Nelson, A. Walsh, M. van Schilfgaarde, and P. R. F. Barnes, *Nanoscale*, 2016, **8**, 6317–6327.
31 M. R. Filip, G. E. Eperon, H. J. Snaith, and F. Giustino, *Nat. Commun.*, 2014, **5**, 5757.
32 B. J. Foley, D. L. Marlowe, K. Sun, W. A. Saidi, L. Scudiero, M. C. Gupta, and J. J. Choi, *Appl. Phys. Lett.*, 2015, **106**, 243904.
33 V. D'Innocenzo, G. Grancini, M. J. P. Alcocer, A. R. S. Kandada, S. D. Stranks, M. M. Lee et al., *Nat. Commun.*, 2014, **5**, 3586.
34 M. I. Saidaminov, A. L. Abdelhady, G. Maculan, and O. M. Bakr, *Chem. Commun.*, 2015, **51**, 17658–61.
35 J. M. Kadro, K. Nonomura, D. Gachet, M. Grätzel, and A. Hagfeldt, *Sci. Rep.*, 2015, **5**, 11654.
36 L. Abdelhady, M. I. Saidaminov, B. Murali, V. Adinolfi, O. Voznyy, K. Katsiev, E. Alarousu, R. Comin, I. Dursun, L. Sinatra, E. H. Sargent, O. F. Mohammed, and O. M. Bakr, *J. Phys. Chem. Lett.*, 2016, **7**, 295–301.
37 M. Luan, J. Song, X. Wei, F. Chen, and J. Liu, *CrystEngComm*, 2016. Advance Article
38 G. Kieslich, S. Sun, and T. Cheetham, *Chem. Sci.*, 2014, **5**, 4712–4715.
39 R. D. Shannon, *Acta Crystallogr. Sect. A*, 1976, **32**, 751–767.
40 Amat, E. Mosconi, E. Ronca, C. Quarti, P. Umari, M. K. Nazeeruddin, M. Grätzel, and F. De Angelis, *Nano Lett.*, 2014, **14**, 3608–16
41 J. H. Lee, N. C. Bristowe, J. H. Lee, S.-H. Lee, P. D. Bristowe, A. K. Cheetham, H. M. Jang, *Chem. Mater.*, 2016, **28**, 4259-4266
42 W. Travis, E. N. K. Glover, H. Bronstein, D. O. Scanlon, and R. Palgrave, *Chem. Sci.*, 2016. Advance Article

This journal is © The Royal Society of Chemistry 20xx

Please do not adjust margins